American Mineralogist, Volume 84, pages 1925–1931, 1999

HRTEM analysis of dislocation cores and stacking faults in naturally deformed biotite crystals

DAVID CHRISTOPHER NOE* AND DAVID R. VEBLEN

Department of Earth and Planetary Sciences, The Johns Hopkins University, Baltimore, Maryland 21218, U.S.A.

ABSTRACT

HTREM images of naturally deformed, mylonitized biotite crystals were examined to determine where deformation-related defects occur in the structure. Dislocations were found to be associated with the plane of oxygen atoms that constitutes the base of the octahedral sheet and the apical plane of the tetrahedral sheet, rather than in the interlayer as has been generally assumed. Consistent with previous investigations, this region was also confirmed as the position at which stacking faults occur. The location of these defects was determined by comparing sub-unit-cell scale fringes in experimental images to simulated images with dislocation cores and stacking faults. Previous investigations have generally relied on indirect techniques and have yielded ambiguous results.

INTRODUCTION

One of the most important variables in the deformation of rocks is the mechanical properties of their constituent minerals. As such, micas are an important class of minerals because they are geologically abundant and because relatively small shear stresses are required for the onset of plastic deformation. Dislocation glide in the (001) basal planes of crystals is ultimately responsible for the easy plastic deformation of micas, regardless of the orientation of compressional axes (Borg and Handin 1966; Etheridge et al. 1973; Bell et al. 1986; Mares and Kronenberg 1993). The strength of foliated rocks is controlled by the volume fraction of mica present and the interconnectivity of mica lenses (Shea and Kronenberg 1993; Wintsch et al. 1995; Borg and Handin 1966); in fact, the strength of rocks in fault zones may approach that of single phyllosilicate crystals if there is a strong preferred orientation and contiguity of mica grains (Wintsch et al. 1995). Because of its importance, considerable work has been devoted to the mechanical deformation of biotite crystals. Although dislocation glide is confined to the basal plane, biotite crystals are highly anisotropic and there are multiple regions within a single unit cell where glide could occur. Both the octahedral sheet and the interlayer have been proposed as the region in which the dislocation cores responsible for deformation are present.

Previous work concerning the placement of dislocations in the biotite structure has generally relied on indirect techniques and produced contradictory results. Additionally, most of the work has been performed on samples that were deformed under laboratory conditions and may not accurately reflect natural processes. Relevant studies include "bend" tests (Mügge 1898; Friedel 1926), analyses of kink banding (Borg and Handin 1966; Hörz and Ahrens 1970; Etheridge et al. 1973; Sanchez-Navas and Galindo-Zaldivar 1993; Bell et al. 1986), partial dislocations (Meike 1989; Christoffersen and Kronenberg 1993; Bell and Wilson 1981), microcleavages (Baños et al. 1983), TEM amplitude-contrast experiments (Meike 1989; Christoffersen and Kronenberg 1993; Bell et al. 1986), stacking faults (Bell and Wilson 1977 and 1981), and deformation experiments (Kronenberg 1990; Mares and Kronenberg 1993; Christoffersen and Kronenberg 1993; Etheridge et al. 1973; Borg and Handin 1966; Noe et al. 1999). To determine the region where dislocation glide occurs in mylonitic rocks, naturally deformed biotite crystals were examined by high-resolution transmission electron microscopy (HRTEM). Analysis of sub-unit-cell scale lattice fringes around defects allowed for a direct determination of where dislocation cores were present in the structures.

THE BIOTITE STRUCTURE

Anions form two different types of planes in the mica structure. The first type is a pseudo-closest-packed plane of anions (referred to here as the hydroxyl plane) that forms the apical plane of anions coordinated to tetrahedral cations, and with an adjacent hydroxyl plane completes the coordination of the octahedral sites. Although anions in the hydroxyl plane maintain a closest-packed geometry, the spacing between them (0.307 to 0.311 nm, in the biotite refinement of Brigatti and Davoli 1990) exceeds that found in many structures with closest-packed oxygen atoms (e.g., approximately 0.258 nm in the spinel structure). The second type of anion plane has been referred to as the "basal plane" of oxygen atoms. Because the term "basal plane" has been used variably to refer to both this anion plane and the (001) plane in general, this anion plane will be referred to as the "basal oxygen plane." The term "basal plane" will be reserved for the (001) plane in general. Pseudo-hexagonal rings are formed by the removal of one third of the oxygen atoms from a plane that could otherwise be envisioned as closest-packed. Oxygen

*Current address: 11869 Wilshire Dr., N. Huntingdon, PA 15642, U.S.A. E-mail: Noed@hwr.com

atoms in the basal oxygen plane complete the four-fold coordination to the tetrahedral cations and are also bonded to interlayer cations. Anion-anion spacings in this plane are much closer to those typically found in closest-packed oxygen planes (0.269 nm, in the refinement of Brigatti and Davoli 1990).

EXPERIMENTAL DETAILS

Sample material and preparation

Naturally deformed biotite crystals were obtained from mylonitic rocks that displayed biotite "fish," a metamorphic texture produced from intense shearing. Source material was obtained from a set of teaching specimens of unknown locality and from samples of the Ruby Mountain mylonite kindly provided by Arthur Snoke (Hurlow et al. 1991; Lister and Snoke 1984). Most crystals had undergone some degree of recrystallization, but un-recrystallized regions were identified based upon textures described by Lister and Snoke (1984). HTREM samples were produced from the un-recrystallized cores of crystals in petrographic thin sections and were thinned by Ar bombardment until specimens of the desired thickness were produced. Samples were examined with the Philips 420ST transmission electron microscope (TEM) located in the Johns Hopkins University Department of Earth and Planetary Sciences, operated at 120 keV, the JEOL 4000EX TEM located in the University of Pennsylvania Laboratory for Research into the Structure of Matter (LRSM), operated at 400 keV, and the 300keV Philips CM300-FEG TEM at the National Institute for Standards and Technology (NIST). The images presented in this paper were obtained with the 420ST; a limitation of this microscope is that cross-fringes are not resolved in [010] and <310> zone axis images. Images are therefore presented only from the [100] and <110> zone axes.

Mechanical damage is always a potential problem arising from the thin-sectioning process, but especially when the object of study is mechanical deformation. Thin sections were produced from the Ruby Mountain mylonite using conventional methods, but care was taken to limit induced deformation by "gentle" use of the grinder and polisher, and by leaving the thin section considerably thicker (~60 μm) than the standard 30 mm. TEM specimens produced from these thin sections required more ion milling than most specimens, but damage produced by ion milling should not mimic the deformation features of concern.

HRTEM image simulations

HRTEM image simulations were calculated to correlate experimentally derived lattice fringes with the underlying atomic structure. These simulations were performed with the EMS set of programs (Stadelmann 1987) and the MacTempas program using standard procedures.

Dislocation simulations were calculated using the MacTempas and CrystalKit programs. These simulations are of limited utility because the strain field around these dislocations cannot be quantified accurately, but they do qualitatively illustrate the effects on different portions of the structure. A portion of the model was compressed along [010] by shortening the *b* axial length by 20%, such that five unit cells fit along a distance formerly occupied by four. Two unit cells of undistorted structure were added to either end of this region (Figs. 1, 2, and 3), creating a unit that formed one side of the hypothetical glide plane. An undistorted portion of the structure was added adjacent to this unit, to form the other side of the glide plane. The rectangular region of distorted contrast in these images is from the shortening of the *b* axial length to create the dislocation core. The area of greatest interest in these features is immediately adjacent to the glide plane; the effect upon images immediately above the glide plane (in the undistorted region of the structure) can be qualitatively assessed. Dislocations were simulated in the interlayer, octahedral sheet, and tetrahedral sheet.

Stacking fault diffraction pattern simulations were performed to determine if streaking in the $k \neq 3n$ diffraction rows could be correlated with the crystallographic location of stacking faults. Crystalkit was used to translate selected portions of the biotite structure model to imitate 1/3[010] stacking faults. Stacking faults were simulated between interlayer cations and the basal oxygen plane and between octahedral cations and the hydroxyl plane. The latter type of stacking fault merely represents a local change in the polytypic sequence. The crystallographic models used to simulate stacking faults are presented in Figure 4.

RESULTS

Defect simulations

Meike (1989) noted that the observed advance of dislocations during dynamic testing of biotite was consistent with an edge character. Based upon this finding and the greater complexity required in screw dislocation models, only edge dislocations were simulated. The simulations (Figs. 1, 2, and 3) suggest that dislocation cores present in the interlayer will disrupt the relatively intense fringes observed in this region, whereas dislocation cores in the octahedral sheet will have little effect on interlayer fringes. Dislocation cores present in the tetrahedral sheet have an intermediate effect upon interlayer fringes, but the fringes still remain distinct and well defined.

Stacking fault simulations produced smeared reflections in [110] axis diffraction patterns for all rows of $k \neq 3n$ (Fig. 5). This confirms that the smeared reflections commonly observed in diffraction patterns can arise through the presence of stacking faults. Although there are slight differences between the simulations, the location of the stacking faults within real crystal structures cannot be inferred from the smearing; this is due to the nonideal nature of real crystals and a loss of resolution in the TEM. The HRTEM simulations (Fig. 6) demonstrate that stacking faults in the octahedral sheet have little effect on fringes in the interlayer, and that stacking faults in the interlayer have little effect on fringes in the octahedral sheet.

HRTEM dislocation analysis

Figure 7A shows an HRTEM image of mylonitized biotite imaged down [100]. Low-angle kink band boundaries are present, as are dislocation networks, stacking faults, and areas of parting. In the upper center of the less magnified view is a dislocation core, and in the lower right is an area of parting. Because this area of parting (microcleavage) coincides with a row of bright fringes, and cleavage has been shown to occur in the interlayer, the bright fringes must coincide with the interlayer. This interpretation is supported by image simula-

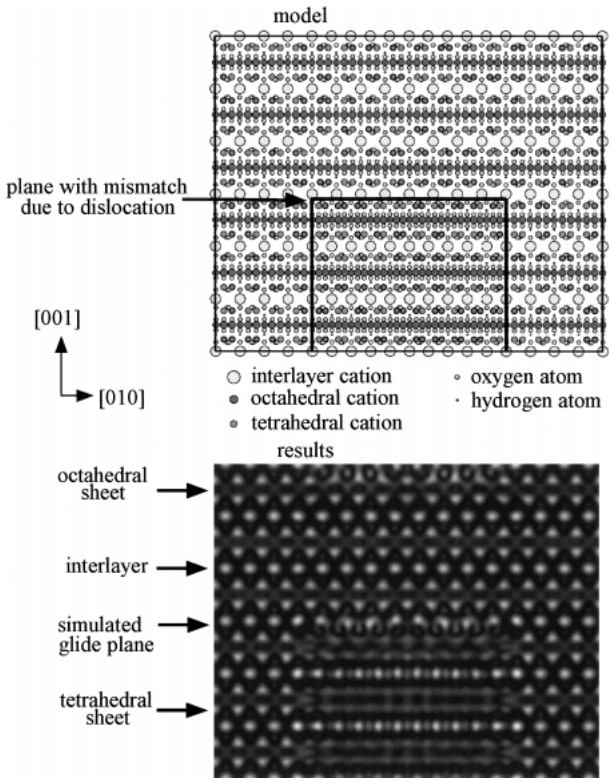

FIGURE 1. Crystallographic model and results for the simulation of a dislocation between the basal oxygen layer and interlayer cations. Note the disrupted fringes in the interlayer region immediately above the simulated glide plane, as was expected for a dislocation here. The region that was compressed to form the dislocation model is outlined with dark lines. Defocus = –73 nm.

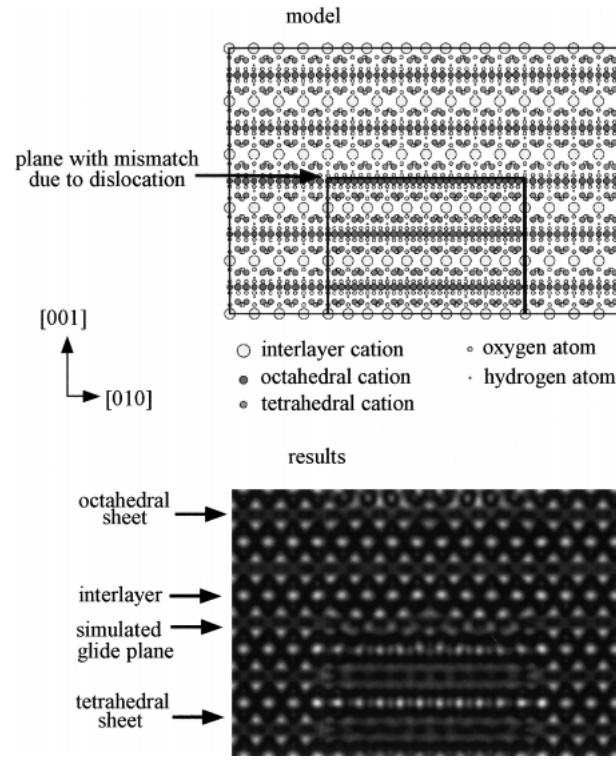

FIGURE 2. Crystallographic model and results for the simulation of a dislocation between the hydroxyl layer and octahedral cations. Note the disrupted fringes in the octahedral and tetrahedral region, as was expected for a dislocation here. The region which was compressed to form the dislocation model is outlined with dark lines. Defocus = –73 nm.

tions. Because dislocation cores are fairly wide in this material (displacement tends to occur over approximately 1 to 2 nm), Burgers circuits must be performed over a relatively large area. Small dots have been placed on the bright fringes in the magnified view to simplify Burgers circuits and to make the dislocation easier to see. These dots are placed in rows along [001] on every fifth cross-fringe along [010]. Where the rows become offset, a dislocation core is present. Dislocations can also be seen by holding the figures at a low angle and sighting along [001]. Examination of the dislocation core reveals that the bright fringes remain relatively undisturbed near the dislocation core, whereas the region between rows of bright basal fringes is greatly distorted. Based upon the image simulations of dislocation cores, the core itself must *not* be present in the interlayer. Interestingly, there is a slight offset of fringes across the (001) plane containing the dislocation (best seen by observing the bright fringes), indicating that the dislocation core is present in a basal plane that also contains a stacking fault.

Figure 7B demonstrates dislocation cores along the edge of a low-angle kink band. In the less magnified view, a network of four dislocations can be seen to the right of the kink band boundary, where the sample has been imaged down [100]. To the left of the boundary, the lattice fringes become fuzzy and indistinct, suggesting that the fold axis is not completely contained within the basal plane. An image simulation is presented at "S" in the less magnified view; the bright fringes in this simulation were found to correspond with the interlayer. The area surrounding the dislocations has been expanded in the magnified view. Once again, dots have been placed on the image to facilitate visualization of the dislocation. As before, the bright fringes remain relatively undisturbed, indicating that the dislocation in *not* in the interlayer. In contrast to Figure 7A, this dislocation is not present in a basal plane containing a stacking fault (no stacking faults are identifiable in this image).

The micrograph in Figure 7C was imaged down [100]. The results are similar to those from previous figures, but the image resolution is slightly better. Little or no disruption of the bright interlayer fringes has occurred. An image simulation is presented adjacent to the "S" in the less magnified view. No stacking faults are apparent in this image.

Figure 7D, taken down <110> from a sample of the Ruby Mountain mylonite, shows a dislocation core and numerous stacking faults. The image simulation present at "S" in the less magnified view confirms that bright fringes correspond with the interlayer. An examination of the magnified view demonstrates that the bright fringes remain relatively undisturbed near the dislocation core, indicating that dislocations in crystals from this locality are not present in the interlayer.

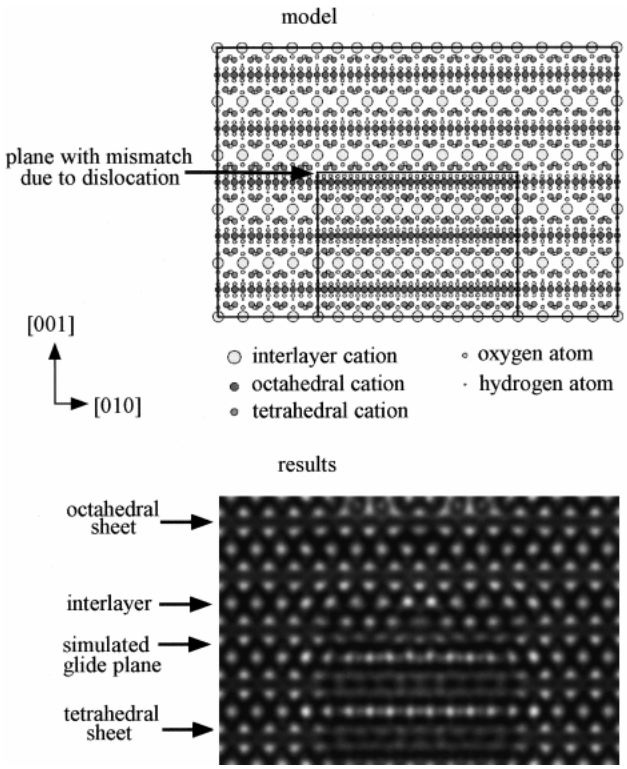

FIGURE 3. Crystallographic model and results for the simulation of a dislocation between the hydroxyl layer and tetrahedral cations. Note the disrupted fringes in the octahedral and tetrahedral region, as was expected for a dislocation here. The region which was compressed to form the dislocation model is outlined with dark lines. Defocus = –73 nm.

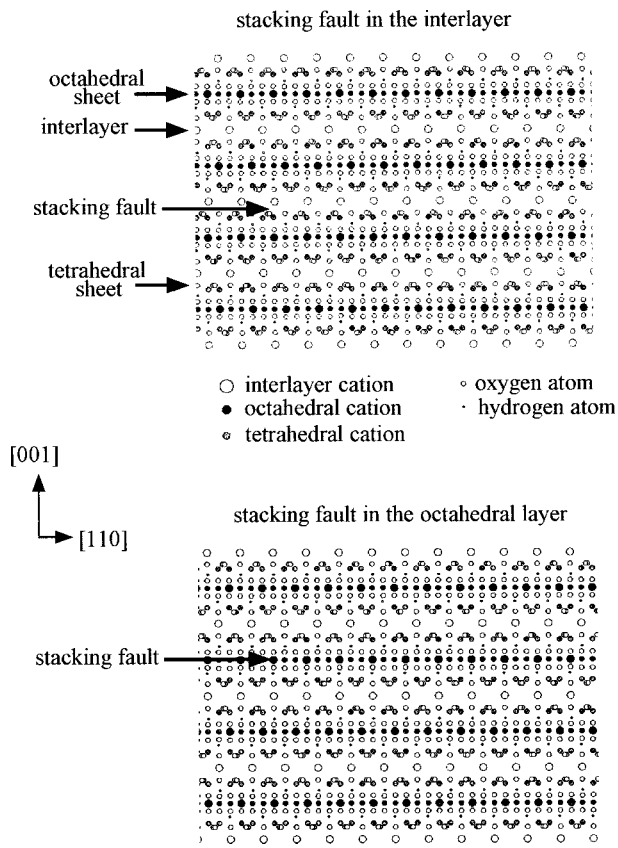

FIGURE 4. Crystallographic models used to simulated stacking faults in the interlayer and the octahedral sheet.

HRTEM stacking fault analysis

The image simulation in the lower right corner of Figure 8 indicates that the interlayer and the basal portion of the tetrahedral sheet form a serrated strip of bright fringes. There is a very high density of stacking faults, indicated by arrows along the left side of the image. Because the original polytypic sequence of this region cannot be identified, one alignment of fringes was arbitrarily chosen as the unfaulted arrangement of the crystal. The offsets due to the stacking faults can be seen to occur between adjacent strips of bright fringes, rather than within the strips themselves. This indicates that the stacking faults must be present between the hydroxyl plane and either the octahedral cation or tetrahedral cation planes. These results partially confirm those of Bell and Wilson (1981), who found that stacking faults were in the octahedral sheet based upon an analysis of defect vectors.

Dislocation amplitude-contrast experiments

Attempts to determine the line directions and Burgers vectors of dislocations were not successful. Other workers have generally reported Burgers vectors parallel to [100] or <110> from dislocation contrast experiments in crystals that were experimentally deformed, leading to an assumption that slip occurred in the interlayer. For comparative purposes, a knowledge of Burgers vectors and line directions was desired for the mylonitic samples; the TEM images, however, contained abundant Moiré fringes and an intense, mottled contrast that made unambiguous identification of dislocations impossible. Noe and Veblen (1999) describe this mottled contrast in greater detail.

DISCUSSION

Because micas are oxide structures, dislocations propagate by disrupting bonds between cations and anions. Dislocation glide has been identified as occurring only within (001) basal planes, indicating that cross-slip and climb processes are not active between adjacent layers. Assuming that cross-slip and climb do not occur within layers either, an analysis of dislocation glide can be simplified to models in which dislocation cores propagate between planes of anions and cations, without a physical break in either plane; this assumes that dislocations will tend to be present in the region through which they can most easily propagate. There are four regions in which dislocation glide could then occur: (1) between the hydroxyl plane and the plane of octahedral cations, (2) between the hydroxyl plane and the plane of tetrahedral cations, (3) between the basal oxygen plane and the plane of tetrahedral cations, or (4) between the basal oxygen plane and the plane of interlayer cations.

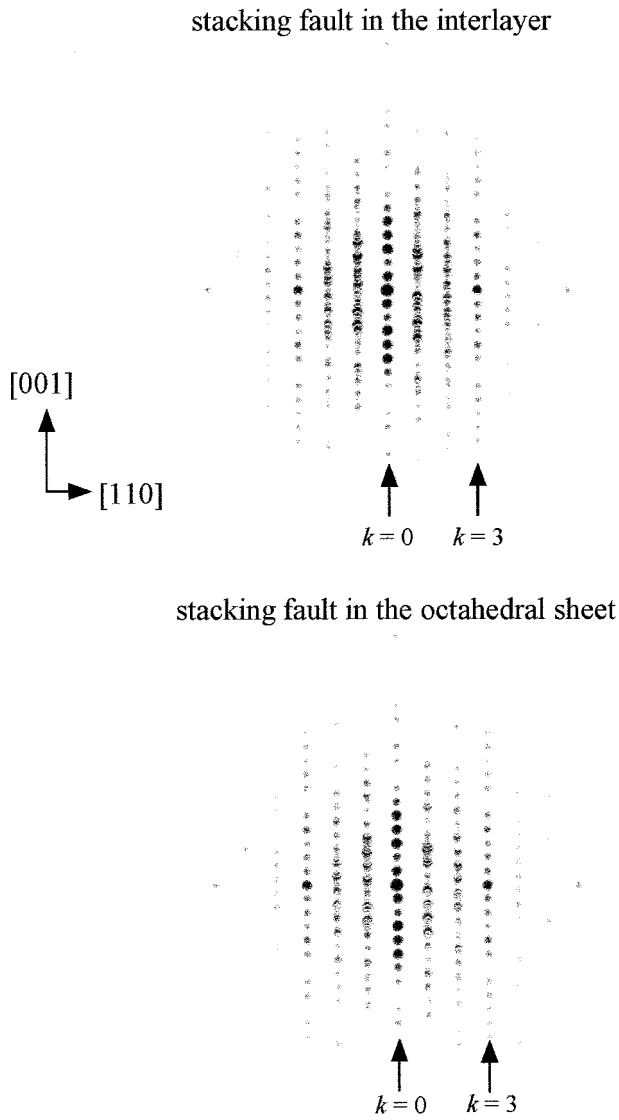

FIGURE 5. Diffraction pattern simulations of stacking faults in the interlayer and octahedral sheet. Notice the smearing of intensity in rows of $k \neq 3n$.

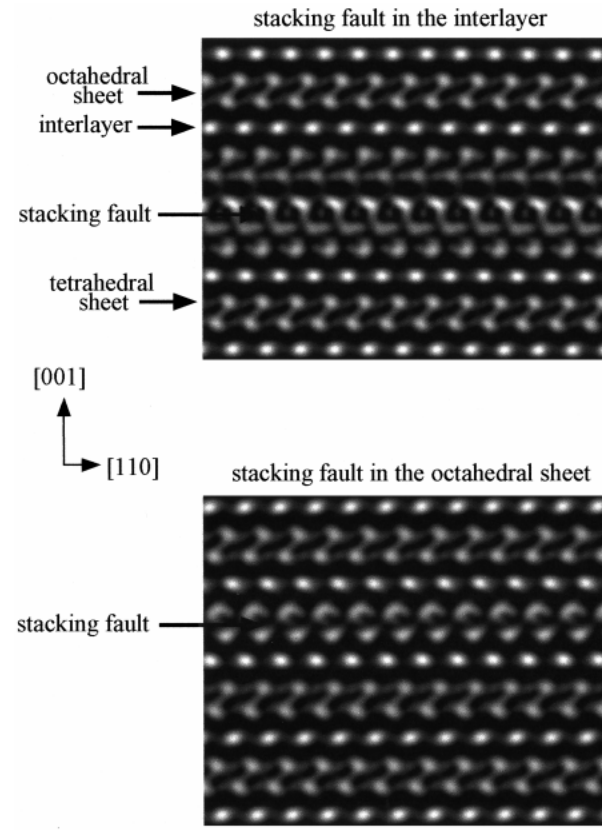

FIGURE 6. Image simulations of stacking faults in the interlayer and octahedral sheet. Stacking faults in the two different regions are easily differentiated by where offsets occur between fringes. Defocus = –73 nm.

The HRTEM analysis indicates that the observed dislocation cores are not consistent with possibility 4 (basal oxygen plane/interlayer cations). The remaining three possibilities could best be evaluated by considering calculations of dislocation glide energies. This type of analysis is exceedingly complex, even for simple metallic structures. Because the strain field around a dislocation core in biotite has not been quantified (although the HRTEM images indicate that it may be relatively large, with considerable disruption in bonding over the width of a few unit-cells), energy calculations are not currently possible. The remaining possibilities can be evaluated, however, based upon an analysis of Burgers vectors and bond strengths.

Peierls-Nabarro type models of dislocation glide have two energy components, accounting for the elastic energy of the dislocation and the misfit energy associated with distorted bonds (Hirth and Lothe 1968). The elastic energy of a gliding dislocation is generally assumed to be constant in these simple models, so the total energy required for glide is controlled by the misfit energy and is a periodic function. If the width of a dislocation is relatively narrow, only a limited number of bonds in the unit cell will be disrupted at any given time, and planes with individually strong bonds will resist glide more than planes with weaker individual bonds. In other words, if the dislocation width is narrow, a hypothetical plane with a few strong bonds may resist dislocation glide more than a plane with numerous weak bonds, even if the sum of the strengths of these weak bonds exceeds that of the strong bonds. This condition arises because a gliding dislocation may not encounter all of the bonds at the same time.

In the case of biotite, however, the HRTEM images suggest that dislocations are relatively wide and disrupt bonding over a width of several unit-cells. Because glide is then affected by all of the bonds in the unit-cell, the plane with the weakest total bonding is an attractive candidate for dislocation glide. This approach does not apply to the interlayer, due to the wide anion rings in the basal oxygen plane; interlayer cations are partially recessed into cavities within these rings. If shear were accommodated by dislocation glide between interlayer cations

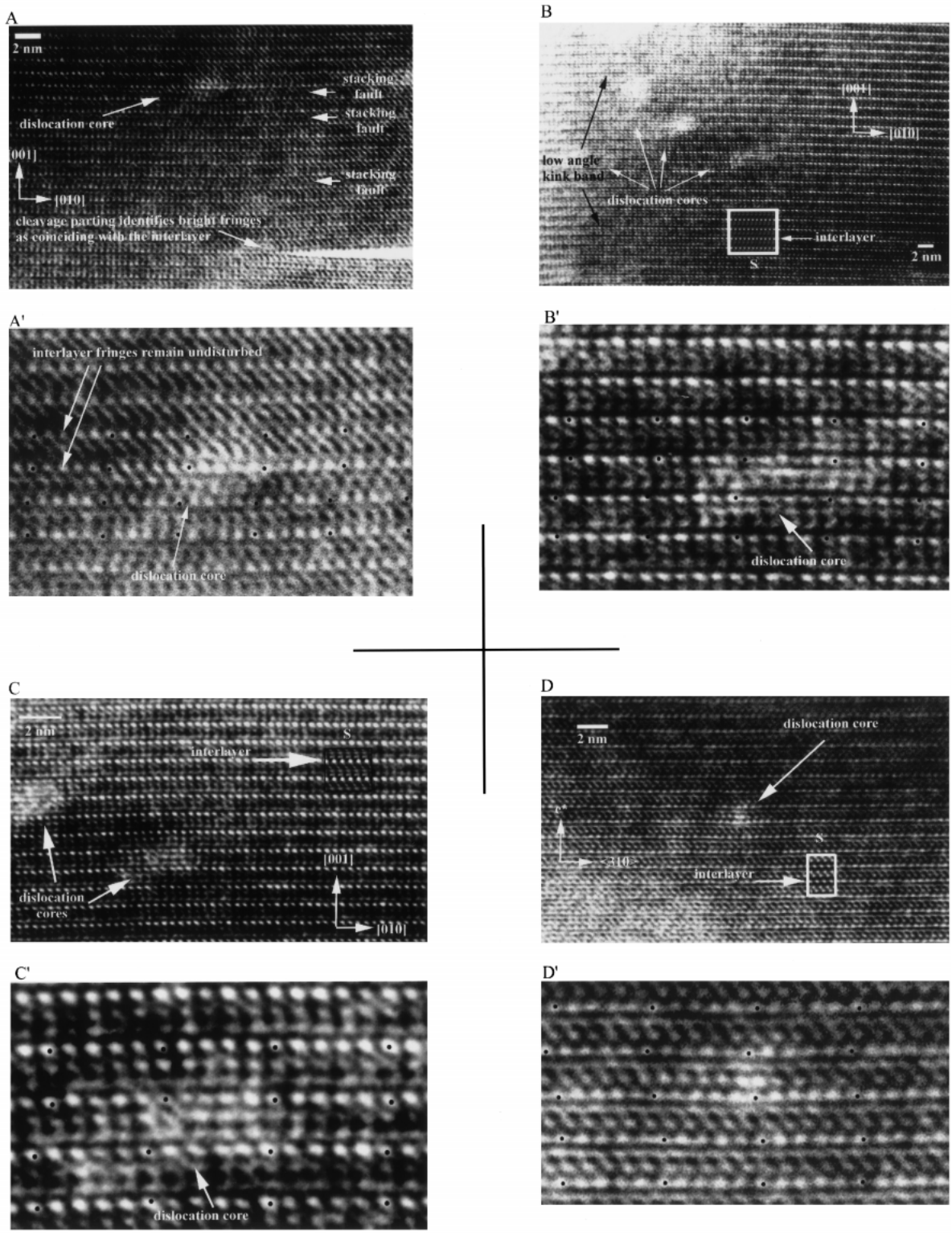

FIGURE 7. Regional (less magnified; unprimed) and magnified (primed) views of dislocation cores in biotite. Stacking faults, low angle kink bands, and cleavage cracks can be seen in many of the images. Image simulations are presented adjacent to the "S" in several of the micrographs. Fringes associated with the interlayer are relatively undisturbed, indicating that the dislocation cores are not in this portion of the structure. Defocus of A(A') = –67 nm, B(B') = –75 nm, C(C') = –63 nm, D(D') = –75 nm. The specimen in D(D') is from the Ruby Mountain mylonite; all others are from the mylonite of unknown provenance. All micrographs were obtained using the Philips 420ST.

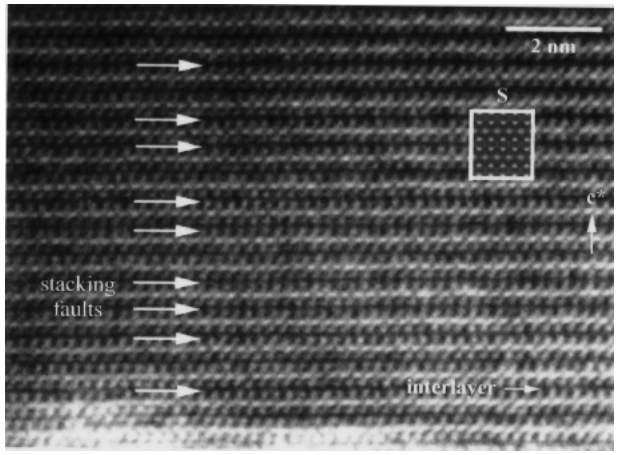

FIGURE 8. Stacking faults in mylonitic biotite. Stacking faults occur between the hydroxyl plane and either the octahedral or the tetrahedral cations. An image simulation is presented at "S"; defocus = –100 nm. Specimen from the Ruby Mountain mylonite, imaged down the <110> axis.

and basal oxygen plane anions without dilatation along [001], interlayer cations would be forced to "plow" their way through the basal oxygen plane, disrupting bonding between anions in this plane and the tetrahedral cations.

The strength of individual bonds can be approximated using Pauling's Second Rule (Pauling 1929), in which the total strength of valency bonds reaching a ligand is equal to the charge of the ligand. For a divalent octahedral cation, the strength of an individual bond is 1/3 valence unit (v.u.). For a single (polytype 1M) unit cell there are 3 octahedral sites, and the total strength of bonds between octahedral cations and anions is 6 v.u. Each octahedral cation is bonded to two hydroxyl planes, so the strength of bonds between octahedral cations and a single hydroxyl plane is 3 v.u.

The total valence of tetrahedral cations in an average unit cell is +15. Each tetrahedral cation is bonded to 4 anions, so the average strength of each bond is 15/16 v.u., which will be approximated as 1 v.u. Each tetrahedral cation is bonded to three anions in the basal oxygen plane, so the average bond strength between a tetrahedral cation and the basal oxygen plane is 3 v.u. There are four tetrahedral cations in a formula unit, divided between two tetrahedral sheets, so the average bond strength between a tetrahedral plane and a basal oxygen plane is 6 v.u.

Each tetrahedral cation is bonded to one anion in the hydroxyl plane, so the average bond strength between a tetrahedral plane and the hydroxyl plane is 2 v.u. A dislocation gliding between the tetrahedral plane and the hydroxyl plane would also disrupt bonding within the OH group of the hydroxyl plane, contributing an extra v.u. The average bond strength disrupted by a dislocation gliding through this region would then be 3 v.u.

These calculations suggest that glide will be favored between the hydroxyl plane and either the octahedral or tetrahedral cations, both of which require the disruption of 3 v.u. per unit-cell. Glide between the basal oxygen plane and tetrahedral cations probably does not occur. Based upon stacking fault defect vectors of 1/3[010], 1/6[310], and 1/6[$3\bar{1}0$], Bell and Wilson (1981) identified the octahedral sheet as the probable location of stacking faults in the biotite structure, because this vector connected nearest-neighbor octahedral cations. However, this is also the expected stacking fault vector caused by the passage of partial dislocations between the hydroxyl plane and tetrahedral cations. The resolution of HRTEM images used in this study was not sufficient to determine whether stacking faults and dislocation cores were in the octahedral or the tetrahedral sheet.

ACKNOWLEDGMENTS

Financial support for this study was provided by NSF grant EAR-9418090 to D.R. Veblen. R. Laskis and P. Davies are thanked for the use of the electron microscope facility at the University of Pennsylvania Laboratory for Research into the Structure of Matter (LRSM), and E. Steel is thanked for the use of the 300keV Philips CM300-FEG TEM at the National Institute for Standards and Technology (NIST). D. Elbert provided the mylonitic sample of unknown origin. This manuscript was improved by reviews from J. Hughes, J. Ferry, D. Peacor, D.R. Peavar, and G. Giovanni.

REFERENCES CITED

Baños, J.O., Amouric, M., De Fouquet, C., and Baronnet, A. (1983) Interlayering and interlayer slip in biotite as seen by HTREM. American Mineralogist, 68, 754–758.

Bell, I.A. and Wilson, C.J.L. (1977) Growth defects in metamorphic biotite. Physics and Chemistry of Minerals, 2, 153–169.

———(1981) Deformation of biotite and muscovite: TEM microstructure and deformation model, Tectonophysics, 78, 201–228.

Bell, I.A., Wilson, C.J.L., McLaren, A.C., and Etheridge, M.A. (1986) Kinks in mica: Role of dislocations and (001) cleavage. Tectonophysics, 127, 49–65.

Borg, I. and Handin, J. (1966) Experimental deformation of crystalline rocks. Tectonophysics, 3, 249–368.

Brigatti, M.F. and Davoli, P. (1990) Crystal structure refinement of 1m plutonic biotites. American Mineralogist, 75, 305–313.

Christoffersen, R. and Kronenberg, A.K. (1993) Dislocation interactions in experimentally deformed biotite. Journal of Structural Geology, 15, 1077–1095.

Etheridge, M.A., Hobbs, B.E., and Paterson, M.S. (1973) Experimental deformation of single crystals of biotite. Contributions to Mineralogy and Petrology, 38, 21–36.

Friedel, G. (1926) Leons de crystallographie. Berger-Levault, Paris.

Hirth, J.P., and Lothe, J. (1968) Theory of Dislocations, p. 201–250. McGraw-Hill, N.Y.

Hörz, F., and Ahrens, T.J. (1970) Deformation of experimentally shocked biotite. American Journal of Science, 267, 1213–1229.

Hurlow, H.A., Snoke, A.W., and Hodges, K.V. (1991) Temperature and pressure of mylonitization in a Tertiary extensional shear zone, Ruby Mountains-East Humboldt Range, Nevada: Tectonic implications. Geology, 19, 82–86.

Kronenberg, A.K., Kirby, S.H., Pinkston, J. (1990) Basal slip and mechanical anisotropy of Biotite. Journal of Geophysical Research, 95, B12, 19257–19278.

Lister, G.S. and Snoke, A.W. (1984) S-C Mylonites. Journal of Structural Geology, 6, 617–638.

Mares, V.M. and Kronenberg, A.K. (1993) Experimental deformation of muscovite. Journal of Structural Geology, 15, 1061–1075.

Meike, A. (1989) In situ deformation of micas: A high-voltage electron-microscope study. American Mineralogist, 74, 780–796.

Mügge, O. (1898) Ueber Translationen und verwandte Erscheinungen in Kristallen. Neues Jahrbuch für Mineralogie, Geologie und Palæontologie, 1, 71–158.

Noe, D.C. and Veblen, D.R. (1999) Mottled contrast in TEM images of mica crystals. American Mineralogist, 84, 1933–1939

Noe, D.C., Veblen, D., LaVan, D.A. (1999) Lap shear testing of biotite and phlogopite crystals and the application of interferometric strain/displacement gages to mineralogy. Journal of Geophysical Research, 104, 17811–17822.

Pauling, L. (1929) The principles determining the structure of complex ionic crystals. Journal of the American Chemical Society, 51, 1010–1026.

Sanchez-Navas, A. and Galindo-Zaldivar, J. (1993) Alteration and deformation microstructures of biotite from plagioclase-rich dykes (Ronda Massif, S. Spain). European Journal of Mineralogy, 5, 245–256.

Shea ,W.T. and Kronenberg, A.K. (1993) Strength and anisotropy of foliated rocks with varied mica contents. Journal of Structural Geology, 15, 1097–1121.

Stadelmann, P. (1987) EMS-a software package for electron diffraction analysis and HREM image simulation in materials science. Ultramicroscopy, 21, 131–145.

Wintsch, R.P., Christoffersen, R., and Kronenberg, A.K. (1995) Fluid-rock reaction weakening of fault zones. Journal of Geophysical Research, 100, B7, 13021–13032.

MANUSCRIPT RECEIVED JUNE 11, 1998
MANUSCRIPT ACCEPTED JULY 10, 1999
PAPER HANDLED BY PETER R. BUSECK